Article

Investigations of the Thermal Parameters of Hybrid Sol–Gel Coatings Using Nondestructive Photothermal Techniques

Łukasz Chrobak [1,*], Dorota Korte [2,*], Hanna Budasheva [2], Mirosław Maliński [1], Peter Rodič [3], Ingrid Milošev [3] and Sylwia Janta-Lipińska [4]

[1] Faculty of Electronics and Computer Science, Koszalin University of Technology, Sniadeckich 2, 75-453 Koszalin, Poland; miroslaw.malinski@tu.koszalin.pl

[2] Laboratory for Environmental and Life Sciences, University of Nova Gorica, Vipavska cesta 13, 5000 Nova Gorica, Slovenia; hanna.budasheva@ung.si

[3] Department of Physical and Organic Chemistry, Jožef Stefan Institute, Jamova cesta 39, 1000 Ljubljana, Slovenia; peter.rodic@ijs.si (P.R.); ingrid.milosev@ijs.si (I.M.)

[4] Faculty of Civil Engineering, Environmental and Geodetic Science, Koszalin University of Technology, Sniadeckich 2, 75-453 Koszalin, Poland; sylwia.janta-lipinska@tu.koszalin.pl

[*] Correspondence: lukasz.chrobak@tu.koszalin.pl (Ł.C.); dorota.korte@ung.si (D.K.)

Abstract: This article presents the results of comparative investigations of thermal parameters of hybrid sol–gel coatings (named TMZ) prepared from tetraethyl orthosilicate and organically modified 3-methacryloxypropyltrimethoxysilane. The coatings were prepared with the addition of zirconium(IV) tetrapropoxide chelated with methacrylic acid. Two series of samples were investigated: the first series, TMZ-I, TMZ-II and TMZ-III, with different amounts of zirconium, and the second series, TMZ-I/Ce, TMZ-II/Ce and TMZ-III/Ce, with the addition of cerium nitrate. The influence of the amount of zirconium and cerium on the thermal parameters of the sol–gel coatings was next analyzed. Two non-destructive and photothermal techniques were used for this purpose: photothermal radiometry (PTR) and beam deflection spectroscopy (BDS). The thermal diffusivity and conductivity of the coatings were extracted from the frequency experiments and are presented and discussed. The two-layer model was applied to interpret the photothermal spectra. The results obtained using these two techniques are compared and discussed.

Keywords: hybrid sol–gel coatings; non-destructive testing; photothermal radiometry; photothermal beam deflection spectrometry; thermal diffusivity; thermal conductivity

1. Introduction

The hybrid materials obtained by the sol–gel methods are composite materials combining properties of organic and inorganic polymer materials. Their major advantage is combining various properties in a coating. Inorganic materials are hard, stiff and thermally stable, whereas organic polymers have good toughness, elasticity and low density [1]. The adjustment of the hybrid sol–gel coating properties for desired application can be achieved by introducing changes in their structure or composition as well as by varying their thickness.

Aluminum and aluminum-based alloys currently attract the most attention of all metals in different fields of industry. This is the consequence of their unique properties that include stiffness, low density and high strength-to-weight ratio. These properties can be further improved by the combination of aluminum with other substances to create its alloys. Unfortunately, such a process decreases its corrosion resistance, making the alloys sensitive to oxidation and pitting processes. Thus, various coating systems are employed to protect these materials under service conditions [2]. It has been reported in previous publications that high corrosion resistance for Al/Al-based alloys can be ensured by coatings with introduced Si/Zr particles which also have a polymerized organic matrix [3,4]. The content

of Zr determines the rate and effectiveness of condensation reaction by influencing on the creation of polycondensed Si species and grouping them in large domains and thus making the corrosion resistance of the coating dependent on Zr content. Additionally, different Zr salts such as chloride, acetate and nitrate are found to be an efficient corrosion inhibitors for Al/Al-based alloys [5,6] since they form different hydroxides such as $Ce(OH)_3$ and $Ce(OH)_4$ in the surface area when an increased local pH is present caused by cathodic reaction of oxygen reduction that occurs in the case of Si/Zr systems. Therefore, the Ce-doped Si/Zr-based hybrid sol–gel coatings with different amounts of zirconium present a great opportunity for research.

Corrosion protective coatings are not only a barrier layer between the object and its environment, but they also act as a protection of small and local areas of exposed substrate. They also stop the spread of damage, minimize electrolyte and water penetration and block corrosion reactions. One of the weak points of protective coatings is the presence of pores or other defects in which the corrosion process is initiated because they act as diffusion paths and allow the aggressive solution to reach the underlying substrate that is not resistant to corrosion [7].

It is seen from the presented results that the TMZ coatings are dense and compact, which consequently makes them attractive materials as anticorrosion protective layers for Al and different Al alloys since they ensure high corrosion resistance even under aggressive environmental conditions. The level of corrosion protection is dependent on the amount of Zr in the coating that determines the process of condensation reaction and influence on the formation of large domain of polycondensed Si species. Unfortunately, TMZ coatings do not contain corrosion inhibitors that enhance the anticorrosion properties of protective layers. Thus, it is necessary to add additional compounds into the coating matrix. The most promising species were found to be rare earth cations such as cerium(III) and cerium(IV) salts, but their addition changes the physical, chemical and corrosion properties of the protective coating.

It has been reported that the thermal properties of hybrid sol–gel also depend on the amount of Zr added to the siloxane network and Ce to the Si/Zr sol [8] since the structure and organization are changed. Thermal properties measured using photothermal beam deflection spectroscopy (BDS) were used to evaluate the porosity of TMZ coatings [8]. Thermal diffusivity and conductivity decreased with the increasing amount of Zr in the coating which is reflected in reduced porosity. TMZ coatings with the amount of Zr showed a better corrosion resistance of NaCl solution. The addition of Ce was beneficial in terms of pinhole blocking and decreasing porosity thus also improving corrosion behavior. In another study, we used BDS to analyze hybrid silica-based acrylic sol–gel coatings with different lengths of alkyl chains [9].

The thermal conductivity and diffusivity of porous materials change with an increase in porosity compared to compact materials [10]. The porosity of such coatings determines their physical properties and thus further possible application. Pores interlink and form cracks, weakening the samples' stability and their resistance to corrosion.

During the last few years, interest in non-destructive testing has increased. Non-destructive photothermal methods have been applied widely in investigating different types of materials [11–13].

The photothermal radiometry (PTR) method [14–17] can be applied to investigations of thermal parameters [18–23], recombination parameters [24,25] or optical parameters [26,27].

This method is non-destructive, the same as the photoacoustic method [28–33], photopyroelectric method [34,35] and beam deflection spectrometry [36–38].

PTR and beam deflection spectroscopy (BDS) have been used in performed investigations of the sol–gel coatings. In this work, photothermal radiometry in the frequency domain was used. The pulse variant of this method is also used elsewhere [39,40].

The goal of the study is to apply the PTR and BDS techniques for precise determination of thermal parameters of hybrid organic–inorganic protective coatings related to their coating protective properties.

2. Experimental

2.1. Materials

As a substrate, 1 mm-thick, 15 mm diameter, flat discs of Al (>99.0%, GoodFellow, Huntingdon, UK) were used.

The sol–gel was prepared using tetraethyl orthosilicate (TEOS: $Si(OC_2H_5)_4$, 99.9%, Aldrich, Munich, Germany), 3-methacryloxypropyltrimethoxysilane (MAPTMS: $H_2C=C$ $(CH_3)CO_2(CH_2)_3Si(OCH_3)_3$, 98%, Sigma, St. Louis, MO, USA), zirconium(IV) tetrapropoxide, (ZTP: $Zr(OCH_2CH_2CH_3)_4$, 70 wt.%, in 1-propanol, Aldrich, St. Louis, MO, USA), methacrylic acid (MAA: $H_2C=C(CH_3)COOH$, 99.0%, Aldrich, Zwijndrecht, The Netherlands) and hydrochloric acid (HCl, >37%, AppliChem, Darmstadt, Germany).

The prepared sol–gels were doped using 0.5 wt.% cerium(III) nitrate hexahydrate ($Ce(NO_3)_3 \cdot 6H_2O$, 99.9%, Sigma, Lyon, France).

2.2. Synthesis

In the present study, three different types of organic–inorganic hybrid coatings were prepared. For that purpose, two sols were used. The first one was a silicon-based sol obtained by mixing TEOS and MAPTMS, whereas the second one was produced by adding MAA to the ZTP. TEOS and MAPTMS were hydrolyzed providing acidic conditions and composed with ZTP and MAA. The hybrid sol–gel solution was thus prepared, and it was further stirred for one hour and aged for 2 days. The coatings prepared in the way described above are denoted as TMZ. The molar ratio of alkoxide precursors TEOS/MAPTMS/ZTP/MAA was 0.18:1:X:0.12, where X was 0.06, 0.12 and 0.48. The molar amounts of H_2O (2.075 mol) and catalyst HCl (0.001 mol) were kept constant. These coatings are denoted as TMZ-I, TMZ-II and TMZ-III, respectively. The details of TMZ coating preparation can be found in Reference [8].

The composition of TMZ coatings was then changed by adding 0.5 wt.% of $Ce(NO_3)_3$ into the sol. The final solution was stirred for 10 min and aged for 1 h. Coatings containing Cr are denoted as TMZ-I/Ce, TMZ-II/Ce and TMZ-III/Ce in this study.

2.3. Samples

The Al substrate was ground underwater with 2400- and 4000-grit SiC emery papers, rinsed with distilled water and cleaned in ethanol using an ultrasonic cleaner for 10 min. The coatings were deposited on the Al substrate using syringes equipped with filters (0.2 μm pore size) and a spin-coater (WS-650-23NPP/LITE/IND, Laurell Technologies, North Wales, PA, USA) rotating at 4000 rpm for 30 s. Then, the coatings were left to rest at ambient temperature for 10 min. After that, they were thermally annealed at 100 °C for one hour on a preheated hotplate in daylight. As a result of the whole procedure, the obtained coatings were highly homogeneous with the thickness of about 10 μm.

3. Methods

3.1. Photothermal Radiometry

Modulated photothermal radiometry (PTR) was the first technique applied to obtain the thermal parameters of the hybrid sol–gel coatings. The experimental setup for the PTR measurements in in the frequency domain of the investigated sol–gel coatings is presented in Figure 1.
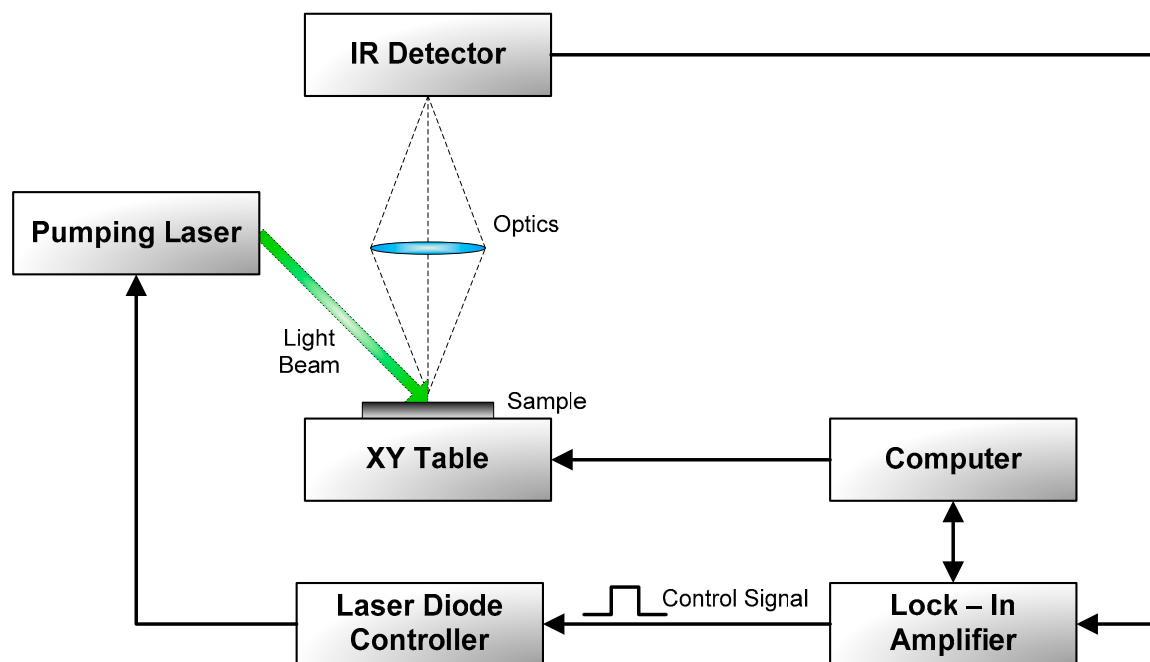
Figure 1. Schematic block diagram of the experimental setup used for the PTR frequency characteristics measurements.

A Roithner LaserTechnik, Vienna, Austria LD-450-1600MG laser diode with a Thorlabs, Newton, NJ, USA, LDM9T/M Laser Diode Mount with integrated temperature controller was used as a light source.

The intensity of the exciting laser light was modulated by a Thorlabs, Newton, NJ, USA, LDC205C Benchtop LD Current Driver. As a result of the optical excitation, thermal waves were generated in the coatings and substrates. The Stanford Research System, Sunnyvale, United States SR830 lock-in amplifier controlled the laser driver. The thermal radiation was detected using a PVI-3TE-5 infrared photovoltaic detector from VIGO System S.A., Warsaw, Poland. The spectral sensitivity range of the used photovoltaic detector was optimized for 5.5 μm. The detector was equipped with a transimpedance amplifier (10 Hz–1 MHz) and cooled with a thermoelectric system. The signal from the photovoltaic detector was collected with a Stanford Research, Sunnyvale, CA, USA, SR 830 phase sensitive amplifier, which measured the amplitude and phase of the PTR signal. The construction of an X-Y table was based on MLA-K modules. They were driven by step motors. All measurements were performed at room temperature and were computer-controlled. The experimental characteristics for investigated samples were measured in the frequency range of modulation of laser light from 10 Hz to 100 kHz.

3.2. Beam Deflection Spectroscopy

The second method for investigating the thermal parameters of coatings was beam deflection spectrometry (BDS). The experimental setup for this method is presented in Figure 2.
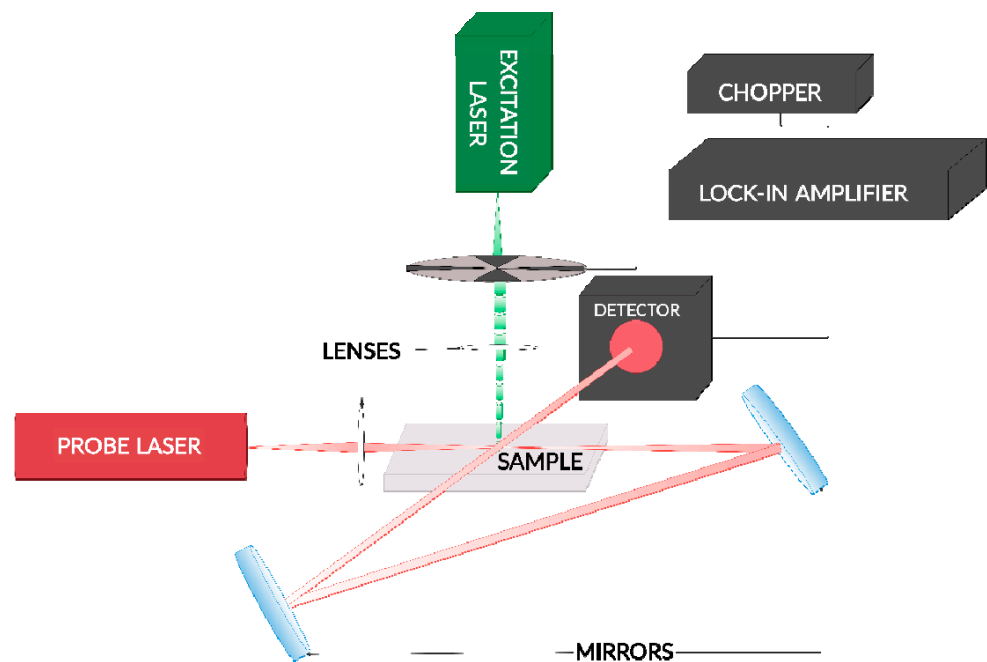
Figure 2. Scheme of the experimental setup used to perform the BDS measurements.

As an excitation beam (EB), a solid-state laser of 532 nm output wavelength and 30 mW output power (Excelsior 532-200 CDRH, LBX-785 HPE, Spectra Physics, Stahnsdorf, Germany) was chosen. A He-Ne laser (1103P, Uniphase, St. Charles, IL, USA) was used as a probe beam (PB) source of 633 nm output wavelength and 3 mW output power. Both beams were focused by a set of lenses (Bi-Convex, AR Coated: 350–700 nm, Edmund Optics, Barrington, NJ, USA). An electro-optic (EO) amplitude modulator (400–600 nm, 4102-M, New Focus, San Jose, CA, USA) controlled by a high voltage amplifier (3211, New Focus, San Jose, CA, USA) and a function generator (JUPITER 2000, Black Star, Longfield, UK) was used to modulate the pump beam to provide the sample's frequency scan from its bulk to subsurface layer and obtain information about its properties distributed within its depth. The range of modulation frequency used in the study was from 2 to 25 kHz. The EB was directed perpendicularly onto the coating's surface and focused to a spot of about 500 μm by a lens of 100 mm focal length (KBX019, Bi-Convex Lens, N-BK7, 6.35 mm Diameter, 25.4 mm EFL, Uncoated, Newport, Irvine, CA, USA).

The PB was focused to a spot of 40 μm in diameter over the coating by a lens of 40 mm focal length (LB1757-A, Thorlabs, Newton, NJ, USA). The intensity change of the probe beam caused by its interaction with temperature oscillation (TO) induced over the coating was measured by QPD (PDQ80A, Thorlabs, Newton, NJ, USA) equipped with a filter (IF) (632.8 nm CWL, Thorlabs, Newton, NJ, USA) and connected to the phase sensitive lock-in amplifier (LiA) (Stanford Research System, Sunnyvale, CA, USA, Model SR510) as well as a PC for data acquisition and processing. The sample was placed on a 3D translation stage (CVI, New Mexico, United States, Model 2480M/2488) which enabled the optimization of the experimental configuration. The BDS experimental setup was optimized by directing the PB twice through the area of TO by a set of mirrors (VIS Dielectric Mirror, 1.0 in. Diameter, 450–700 nm, Newport, Irvine, CA, USA), thus increasing the length of PB interaction with TO and further increase in the sensitivity of the technique.

3.3. Scanning Electron Microscope

The analysis of coating morphology was performed using a scanning electron microscope (SEM) (JSM 7001, JEOL, Tokyo, Japan) equipped with a lower electron detector. The parameters of the microscope were as follows: current 8–10 nA, voltage 15 kV, beam

diameter 1 μm, decreased vacuum in the chamber with the pressure of 50 Pa. Before the analysis, the surface of the coating was coated with 5 nm Au/Pd to avoid charging.

4. Theoretical Background

4.1. PTR Method

Photothermal radiometry is a photothermal technique that relies on thermal wave generation [41–43]. In this method, the sample is illuminated with an intensity-modulated beam of laser light. As a result of the optical absorption of this light, periodical temperature waves arise. For the IR opaque samples, the PTR signal is proportional to the temperature of the illuminated surface of the sample. The investigated samples consisting of two layers (sol–gel coating deposited on aluminum substrate) were coated with a thin (a few nanometers) layer of gold (Figure 3).
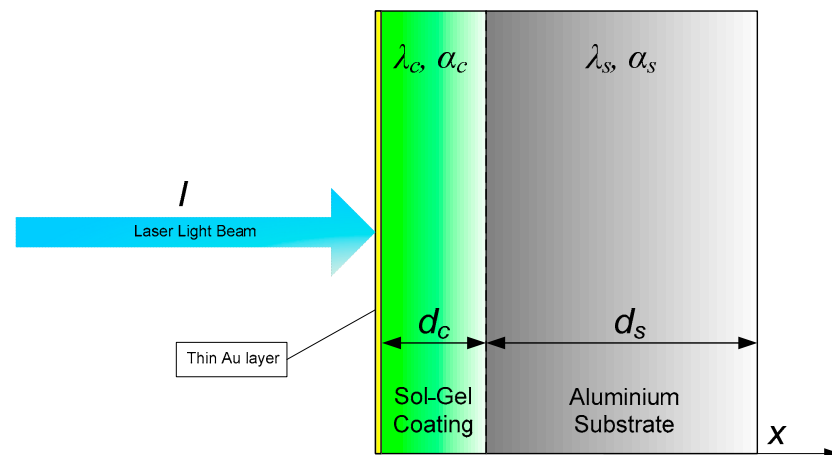

Figure 3. Simplified schematic of the investigated sample.

The gold layer was used in SEM measurements. The presence of gold also assured the role of an absorber in further studies using the PTR method. This allowed the use of a two-layer PTR model presented in Equation (1).

$$T = \frac{I}{\lambda_c \sigma_c} \frac{\cos h(d_c \sigma_c + d_s \sigma_s) + R_{12} \cos h(d_c \sigma_s - d_c \sigma_s)}{\sin h(d_c \sigma_c + d_s \sigma_s) + R_{12} \sin h(d_c \sigma_c - d_s \sigma_s)} \tag{1}$$

where:

I—laser light intensity;

R_{12}—thermal reflection coefficient between the first (coating) and the second (substrate) layer;

d_c—thickness of the coating;

d_s—thickness of the substrate;

λ_c—thermal conductivity of the coating;

α_c—thermal diffusivity of the coating;

λ_s—thermal conductivity of the substrate;

α_s—thermal diffusivity of the substrate.

The thermal reflection coefficient is described by Equation (2):

$$R_{12} = \frac{\frac{\lambda_c}{\sqrt{\alpha_c}} - \frac{\lambda_s}{\sqrt{\alpha_s}}}{\frac{\lambda_c}{\sqrt{\alpha_c}} + \frac{\lambda_s}{\sqrt{\alpha_s}}} \tag{2}$$

The complex thermal wave number (σ_i, subscript i can be s and c which refers to the coating and the substrate, respectively) is described by Equation (3):

$$\sigma_i = (1+i)\sqrt{\frac{\pi f}{\alpha_i}} \tag{3}$$

The amplitude of the photothermal signal is calculated from the equations presented below:

$$Amp = |T| \tag{4}$$

$$Ph = \frac{180}{\pi}\arg(T) \tag{5}$$

In the proposed two-layer model, simulation calculations were performed. The purpose of these calculations was to identify PTR signal changes as a function of changes in thermal diffusion and thermal conductivity values of the coating. The values of parameters taken for the simulation calculations were as follows: $d_c = 10 \times 10^{-4}$ cm, $d_s = 0.05$ cm, $\alpha_c = 5.0 \times 10^{-3}$ cm^2/s, $\lambda_c = 2.0 \times 10^{-3}$ W/cm·K, $\alpha_s = 0.973$ cm^2/s, $\lambda_s = 2.37$ W/cm·K. The results of simulations are presented in Figure 4.
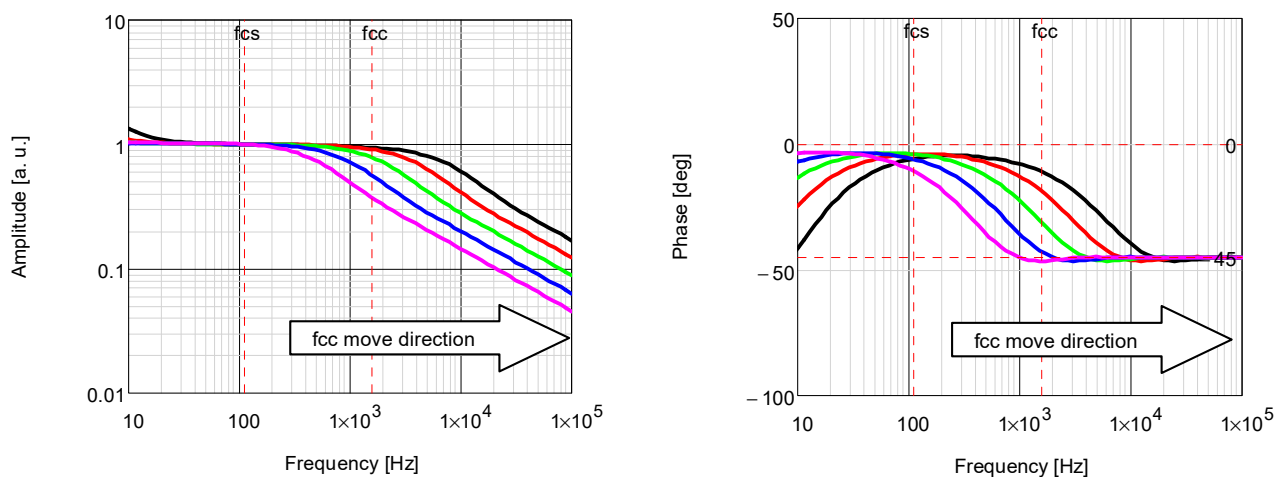

Figure 4. Theoretical PTR amplitude and phase characteristics calculated for different values of thermal parameters. Solid green line (α_c, λ_c), solid red line ($2 \times \alpha_c$, $2 \times \lambda_c$), solid black line ($4 \times \alpha_c$, $4 \times \lambda_c$), solid blue line ($\alpha_c/2$, $\lambda_c/2$) and solid pink line ($\alpha_c/4$, $\lambda_c/4$).

The characteristic frequency for the coating (f_{cc}) and the substrate (f_{cs}) for which the thermal wave diffusion length is equal to the thickness of the coating or the substrate, respectively, can be expressed as follows:

$$fci = \frac{\alpha_i}{\pi d_i} \tag{6}$$

With an increase in the thermal conductivity and the thermal diffusivity of the coating, the corresponding value of the characteristic frequency for the coating (f_{cc}) moves towards higher frequencies. This situation is presented in Figure 4.

4.2. BDS Method

The structure of the examined sample (coating deposited on the bulk substrate with an infinite column of air over it) is presented in Figure 5.
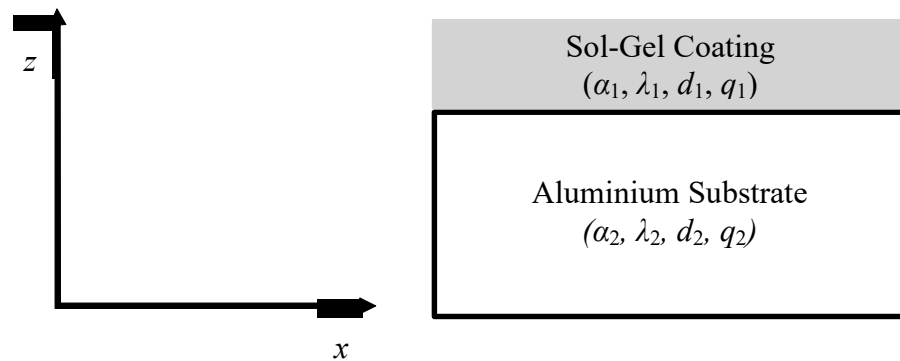
Figure 5. Schematic of the sample geometry for BDS investigation.

In the BDS method, an intensity-modulated excitation beam (EB) of light illuminates the surface of the examined coating [44–46]. As a result of nonradiative de-excitation processes of the absorbed radiation, temperature oscillation (TO) in the coating and fluid over its surface are generated.

The TO in *i*-th layer of the sample (Figure 5) satisfies the Fourier–Kirchhoff equation [42–44]:

$$\frac{1}{\alpha_i}\frac{\partial \vartheta_i}{\partial t} = \nabla^2 \vartheta_i + \frac{q_i}{\lambda_i}; \tag{7}$$

where q_i is the power density of internal heat sources, λ_i is thermal conductivity and α_i is thermal diffusivity.

In our case, the EB is a laser with Gaussian intensity distribution modulated by angular frequency ω; thus, the density of internal heat sources in the *i*-th sample layer can be written as:

$$q_{si}(y,z,t) = \frac{\lambda_i P_0}{4\pi\alpha^2}\sum_1^{i-1}(1-R_k)\exp\left[-\frac{y^2+z^2}{\alpha^2}-\lambda_i\left(z-\sum_1^{i-1}d_k\right)\right][1+\cos(\omega t)] \tag{8}$$

where P_0 is the EB intensity at the input of the experimental setup, d_k is the thickness of the sample layer and R_k is the reflectivity of the sample layer.

The real part of the solution of Equation (7) can be written as:

$$v_f(y,z,t) = \theta(y,z)\cos[\omega t + \varphi(y,z)] \tag{9}$$

where $\theta(y,z)$ is the amplitude TO in the fluid above the coating, and $\varphi(y,z)$ is the phase shift between the coating surface temperature and the EB. $\theta(y,z)$ and $\varphi(y,z)$ contain information about the thermal properties of the coating since they determine the heat conduction within the material and its exchange with the surroundings (structural, transport, optical etc.).

The induced TO is probed by the PB laser beam grazing the coating surface, which causes its intensity change that further produces the photodeflection signal (PDS). The PDS is found based on complex ray theory [44], according to which PB interaction with TO in the fluid above the coating changes the PB trajectory [44–46]:

$$z_1(\xi,\tau) = n_0^2 s_T \int_0^\tau (\tau - \tau')\frac{\partial \vartheta_f}{\partial z}d\tau' \tag{10}$$

where n_0 is the refracting index of undisturbed fluid, $\partial v_f/\partial z$ are temperature gradients induced by TO in the fluid over the coating's surface, $s_T = (1/n_0)(dn/dT)$ is the temperature coefficient of refractive index (thermal sensitivity), τ is the running complex coordinate along the PB trajectory and ξ is the PB's coordinate in the input plane of the experimental setup ($z = 0$).

The consequence of the PB deflection on refractive index gradients changes its divergence which introduces correction to the PB amplitude a_1 in a form:

$$A(x_D) = A_0[1 + a_1(x_D)] \tag{11}$$

where A_0 is the amplitude of the undisturbed probe beam.

Another effect of the PB interaction with TO is the change in the PB optical path that results from both the PB deflection on thermal gradients and the change in the refractive index of the fluid in which it propagates, which introduces the correction to the PB phase:

$$\Phi_1 = kn_0^2 s_T \int_0^\tau \vartheta_f \left[z(\tau') \right] d\tau' \tag{12}$$

The amplitude and phase change of PB results in its intensity change of the photodiode signal given by:

$$S_{PD} = 2K_d \left(\int_0^{+\infty} - \int_{-z0}^{0} \right) dz \int_{-\infty}^{+\infty} dy [\mathrm{Re}(a_1) - k\mathrm{Im}(\Phi_1)]I_0 = A_{PD} \cos\left(\Omega t + \phi_f + \phi_{PD} \right) \tag{13}$$

Here K_d is the detector constant, k is the wavenumber of the PB, I_0 is the light intensity of the undisturbed PB, A_{PD} is the change in PB amplitude and φ_f and φ_{PD} are the change in PB phase resulting from the change in the fluid refractive index because of TO and deflection of PB on thermal gradients, respectively.

Figures 6 and 7 present the amplitude and phase dependence on the coating thermal conductivity (Figure 6) and diffusivity (Figure 7) for TO propagation in air ($\alpha_f = 0.224$ cm^2/s, $\lambda_f = 0.26 \times 10^{-3}$ W/cm·K).
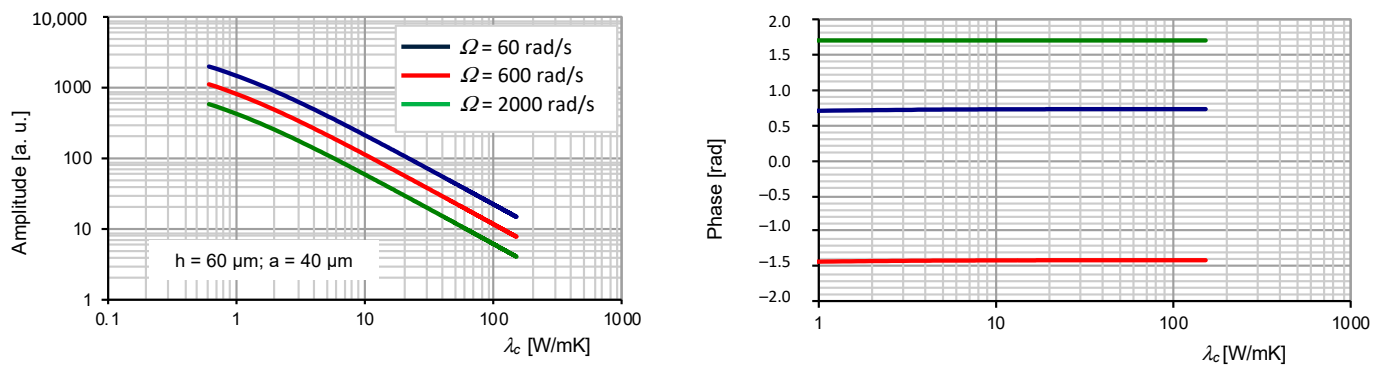

Figure 6. Theoretical BDS amplitude and phase dependence on the values of thermal conductivity of coating deposited on bulk support for PB height over the sample of 60 μm and its radius in the waist of 40 μm and for different modulation frequencies of the excitation beam (60, 600, 2000 rad/s).

The amplitude of BDS signal decreases with the increase in the coating thermal conductivity, whereas the phase weakly depends on it. Thermal conductivity determined the material's ability to conduct heat. The higher the value, the higher the rate of heat transfer decreasing the BDS signal (Figure 6). Thermal diffusivity determines the rate at which the heat generated in the sample is transferred to the surrounding media by diffusion. Thus, the increase in thermal diffusivity value increases the BDS signal, as shown in Figure 7. The behavior of TO is determined by both values of thermal parameters describing their temporal and spatial behavior.
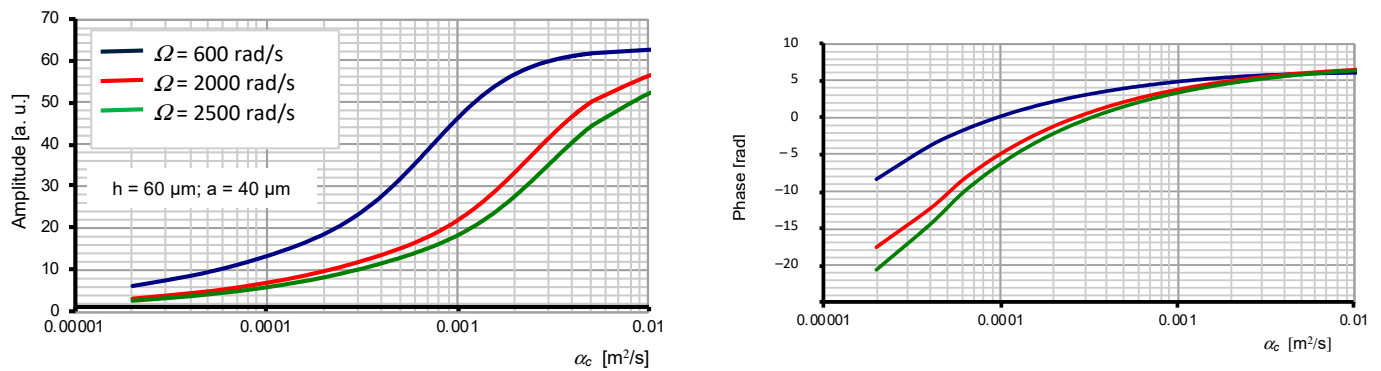
Figure 7. Theoretical BDS amplitude and phase dependence on the values of thermal diffusivity of coating deposited on bulk support for PB height over the sample of 60 μm and its radius in the waist of 40 μm and for different modulation frequencies of the excitation beam (60, 600, 2000 rad/s).

5. Results

Thermal properties of samples were determined using the PTR and BDS techniques and were supported using SEM that provided information about the structure of the coatings.

5.1. SEM Analysis

Morphology of the coatings was obtained by using SEM at magnifications of 5000× as well as 250,000×, as shown in Figures 8 and 9.
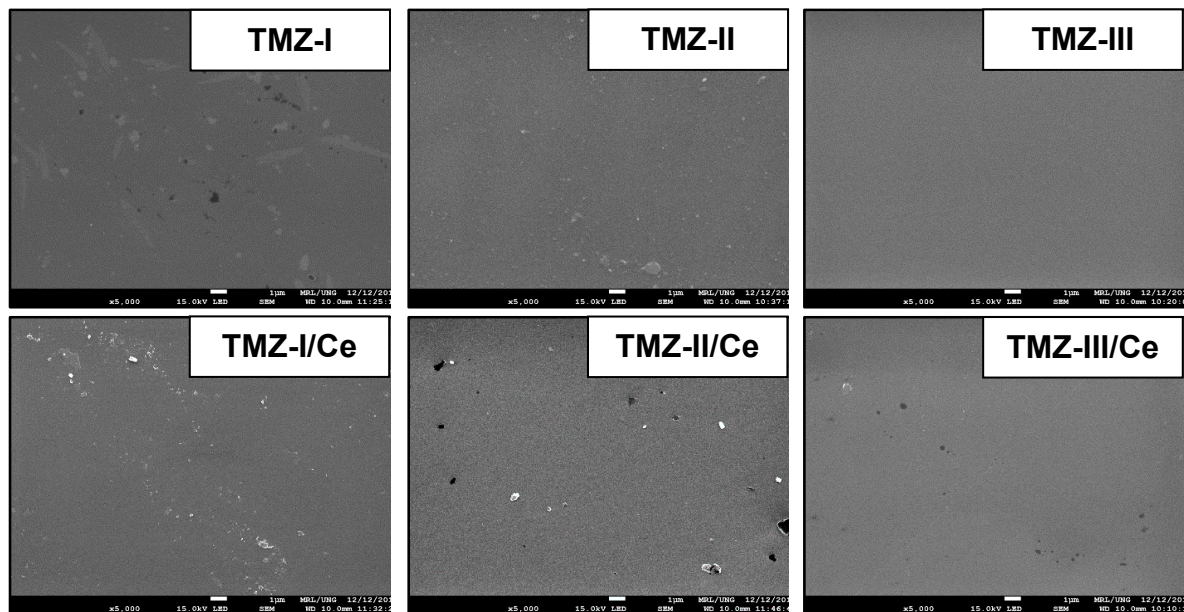

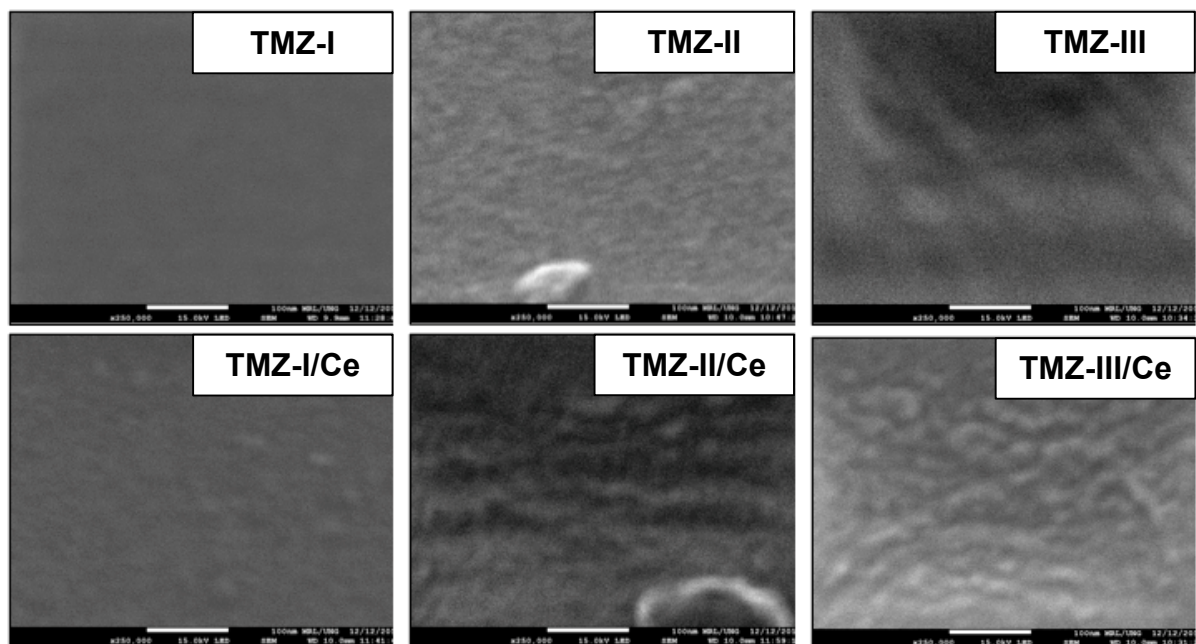
Figure 8. The SEM images (5000×) of the TMZ coatings.

Figure 9. The SEM images (250,000×) of the TMZ coatings.

It is seen from the SEM images that the surfaces of the TMZ coatings are compact and dense without any visible defects, pores or micro-cracks. The homogeneity was further improved with the increase in the amount of zirconium in the coating, which is the result of the presence of more viscous sol due to incorporating zirconium into the sol–gel network [1]. The homogeneity also indicates that the zirconium was fully integrated into the TMZ coating structure and forms a network with Zr and Si. All coatings uniformly cover the aluminum surface, which indicates good adhesion.

Nevertheless, TMZ-I and TMZ-II coatings present a slightly corrugated surface that may be related to the lower condensation degree between initial precursors in the sol during the process of coating preparation [1]. In the case of TMZ-III, coatings appear to be entirely homogeneous, which indicates their higher condensation degree compared to TMZ-I and II. The presence of light spikes in the images of samples doped with Ce (TMZ-x/Ce) confirm implantation. Cerium replaced the non-condensed species in the coatings forming more species with two oxygen bridges and silicon [8].

In the next step, the microscope's magnification was further increased to perform imaging at a magnification of 250,000×. The obtained images are shown in Figure 9.

The images show that the samples specified as the siloxane coating with a higher amount of Zr are more compact and dense materials with higher homogeneity.

5.2. PTR Analysis

The PTR experimental and theoretical amplitude and phase frequency characteristics of the TMZ-I sample are presented in Figure 10.

The solid red line (Theoretical 1) was calculated for the best fit values of thermal parameters (α_c = 2.404 ± 0.073 cm^2/s, λ_c = 2.730 ± 0.168 W/cm·K). The solid green line (Theoretical 2) was calculated for the best fit values of thermal parameters divided by 4 ($\alpha/4$, $\lambda/4$). The solid blue line (Theoretical 3) was calculated for the best fit values of thermal parameters multiplied by 4 ($4 \times \alpha$, $4 \times \lambda$). Circles are experimental data.
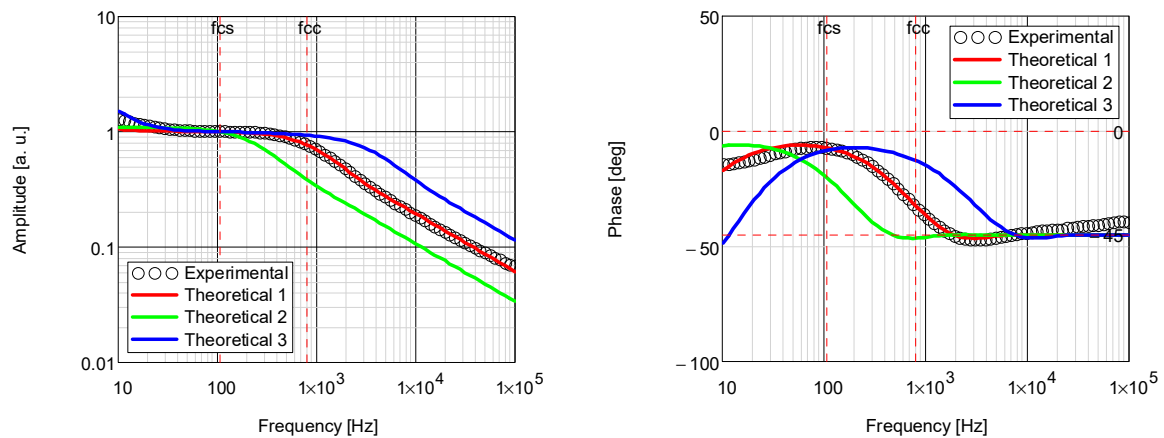
Figure 10. Theoretical and experimental PTR amplitude and phase characteristics obtained for the TMZ-I sample.

The PTR experimental and theoretical amplitude and phase frequency characteristics of the TMZ-I + Ce(NO$_3$)$_3$ sample are presented in Figure 11.
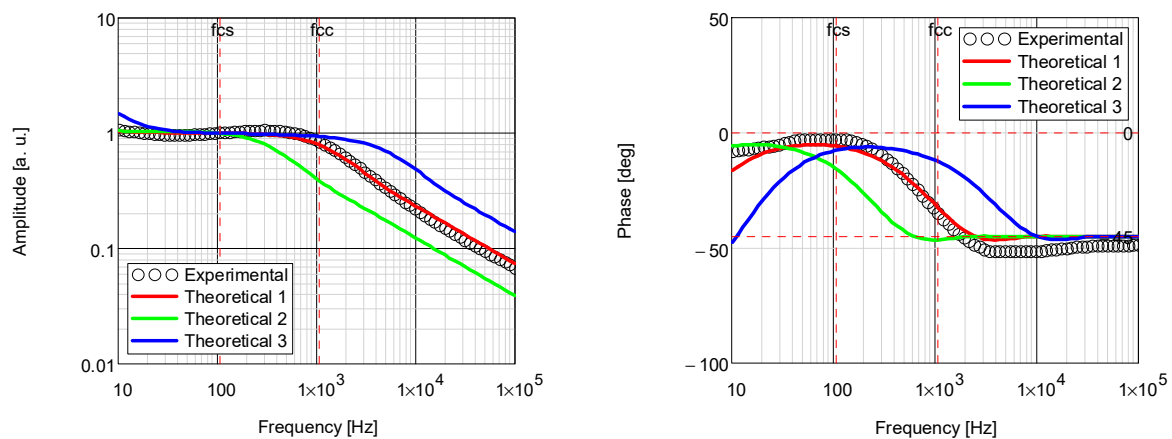

Figure 11. Theoretical and experimental PTR amplitude and phase characteristics obtained for the TMZ-I + Ce(NO$_3$)$_3$ sample.

The solid red line (Theoretical 1) was calculated for the best fit values of thermal parameters ($\alpha_c = 2.140 \pm 0.078$ cm^2/s, $\lambda_c = 2.090 \pm 0.250$ W/cm·K). The solid green line (Theoretical 2) was calculated for the best fit values of thermal parameters divided by 4 ($\alpha/4$, $\lambda/4$). The solid blue line (Theoretical 3) was calculated for the best fit values of thermal parameters multiplied by 4 ($4 \times \alpha$, $4 \times \lambda$). Circles are experimental data.

The PTR experimental and theoretical amplitude and phase frequency characteristics of the TMZ-II sample are presented in Figure 12.
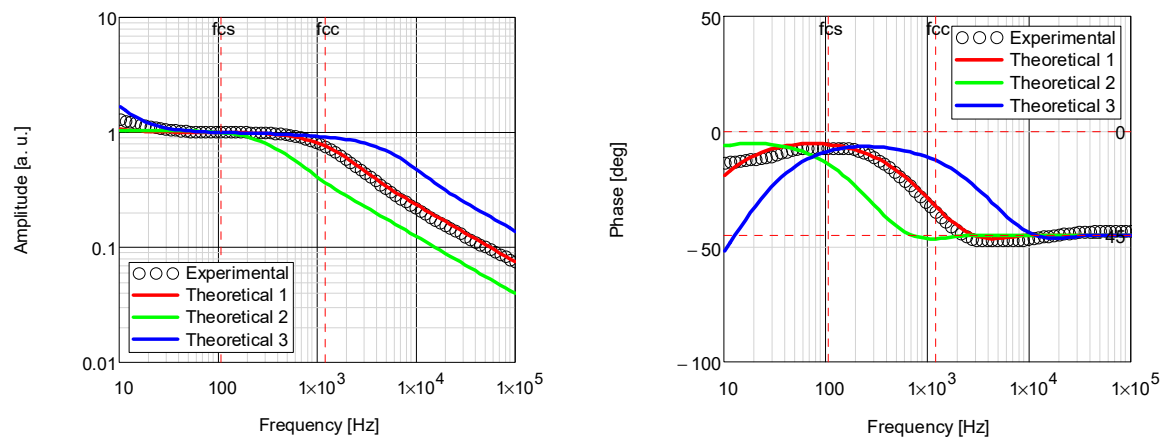
Figure 12. Theoretical and experimental PTR amplitude and phase characteristics obtained for the TMZ-II sample.

The solid red line (Theoretical 1) was calculated for the best fit values of thermal parameters ($\alpha_c = 2.342 \pm 0.060$ cm^2/s, $\lambda_c = 2.523 \pm 0.117$ W/cm·K). The solid green line (Theoretical 2) was calculated for the best fit values of thermal parameters divided by 4 ($\alpha/4$, $\lambda/4$). The solid blue line (Theoretical 3) was calculated for the best fit values of thermal parameters multiplied by 4 ($4 \times \alpha$, $4 \times \lambda$). Circles are experimental data.

The PTR experimental and theoretical amplitude and phase frequency characteristics of the TMZ-II + Ce(NO$_3$)$_3$ sample are presented in Figure 13.
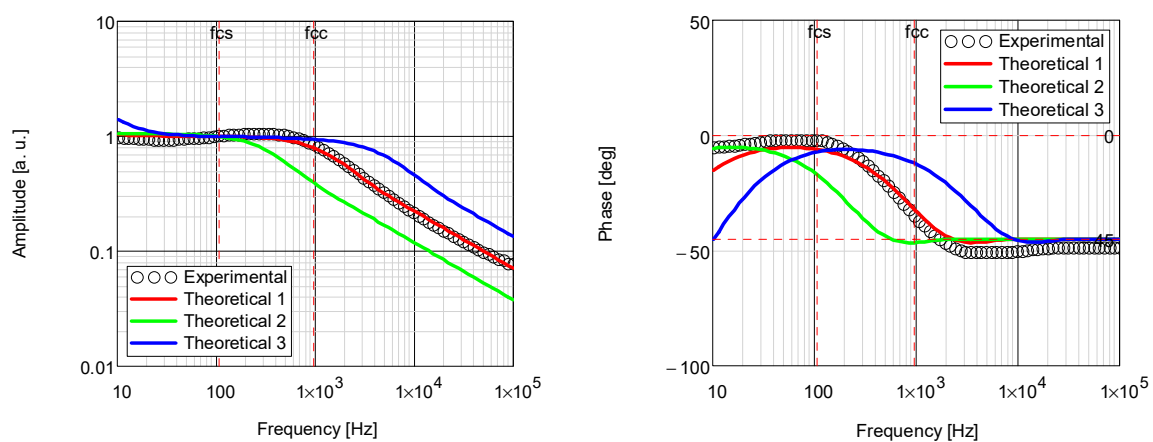

Figure 13. Theoretical and experimental PTR amplitude and phase characteristics obtained for the TMZ-II + Ce(NO$_3$)$_3$ sample.

The solid red line (Theoretical 1) was calculated for the best fit values of thermal parameters ($\alpha_c = 1.960 \pm 0.082$ cm^2/s, $\lambda_c = 1.900 \pm 0.250$ W/cm·K). The solid green line (Theoretical 2) was calculated for the best fit values of thermal parameters divided by 4 ($\alpha/4$, $\lambda/4$). The solid blue line (Theoretical 3) was calculated for the best fit values of thermal parameters multiplied by 4 ($4 \times \alpha$, $4 \times \lambda$). Circles are experimental data.

The PTR experimental and theoretical amplitude and phase frequency characteristics of the TMZ-III sample are presented in Figure 14.
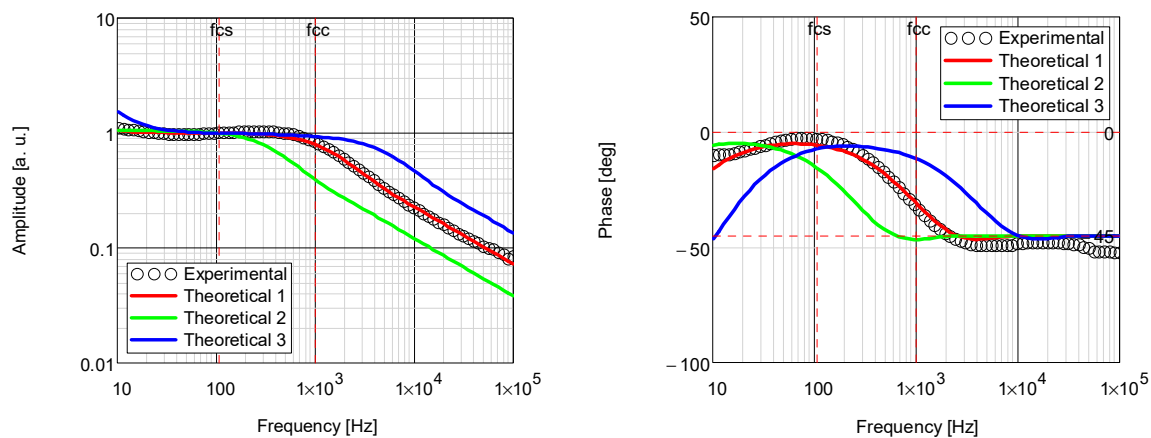
Figure 14. Theoretical and experimental PTR amplitude and phase characteristics obtained for the TMZ-III sample.

The solid red line (Theoretical 1) was calculated for the best fit values of thermal parameters ($\alpha_c = 2.112 \pm 0.057$ cm^2/s, $\lambda_c = 2.100 \pm 0.194$ W/cm·K). The solid green line (Theoretical 2) was calculated for the best fit values of thermal parameters divided by 4 ($\alpha/4$, $\lambda/4$). The solid blue line (Theoretical 3) was calculated for the best fit values of thermal parameters multiplied by 4 ($4 \times \alpha$, $4 \times \lambda$). Circles are experimental data.

The PTR experimental and theoretical amplitude and phase frequency characteristics of the TMZ-III + Ce(NO$_3$)$_3$ sample are presented in Figure 15.
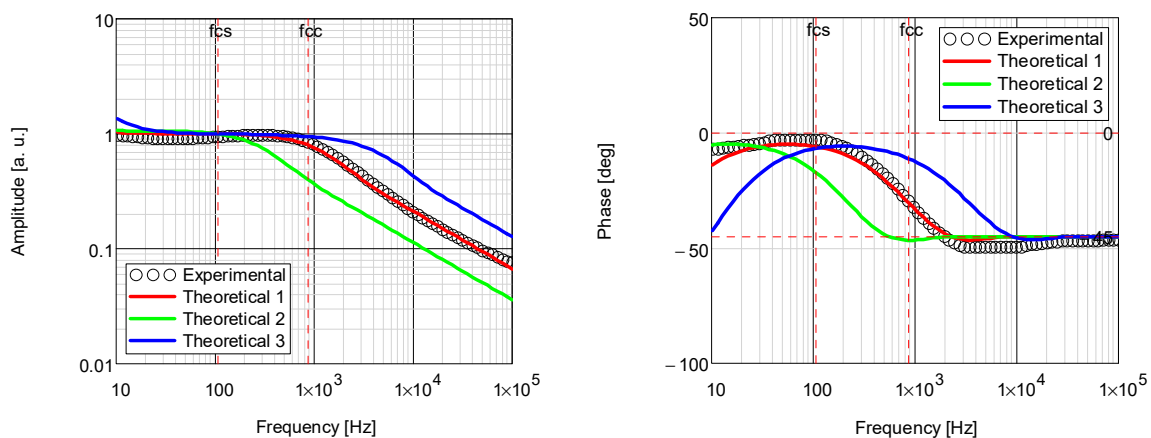
Figure 15. Theoretical and experimental PTR amplitude and phase characteristics obtained for the TMZ-III + Ce(NO$_3$)$_3$ sample.

The solid red line (Theoretical 1) was calculated for the best fit values of thermal parameters ($\alpha_c = 1.838 \pm 0.070$ cm^2/s, $\lambda_c = 1.710 \pm 0.167$ W/cm·K). The solid green line (Theoretical 2) was calculated for the best fit values of thermal parameters divided by 4 ($\alpha/4$, $\lambda/4$). The solid blue line (Theoretical 3) was calculated for the best fit values of thermal parameters multiplied by 4 ($4 \times \alpha$, $4 \times \lambda$). Circles are experimental data.

The thermal diffusivity and conductivity values obtained for investigated samples hold within the relative expanded uncertainties with 95.45% ($\pm 2\sigma$) confidence level [47,48]. They are presented in Table 1.

**Table 1.** Thermal parameters values for investigated TMZ coatings were determined using nondestructive photothermal radiometry.

Coating	Thermal Diffusivity $\times$ 10^{-3} (cm^2/s)	Thermal Conductivity $\times$ 10^{-3} (W/cm·K)
TMZ-I	2.404 ± 0.073	2.730 ± 0.168
TMZ-I/Ce	2.140 ± 0.078	2.090 ± 0.250
TMZ-II	2.342 ± 0.060	2.523 ± 0.117
TMZ-II/Ce	1.960 ± 0.082	1.900 ± 0.250
TMZ-III	2.112 ± 0.057	2.100 ± 0.194
TMZ-III/Ce	1.838 ± 0.070	1.710 ± 0.167

These obtained values were estimated using the best fits of Equation (1) to the normalized experimental data with the use of the least-squares method (multi-parameter fittings).

5.3. BDS Analysis

The amplitude and phase of the BDS signal were acquired as a function of the modulation frequency of TO. The theoretical dependences obtained based on Equations (10)–(13) were fitted to experimental data (Figure 16) using a multiparameter fitting procedure. The fitted parameters were the thermal diffusivity and conductivity of the TMZ coating. The obtained values are presented in Table 2.
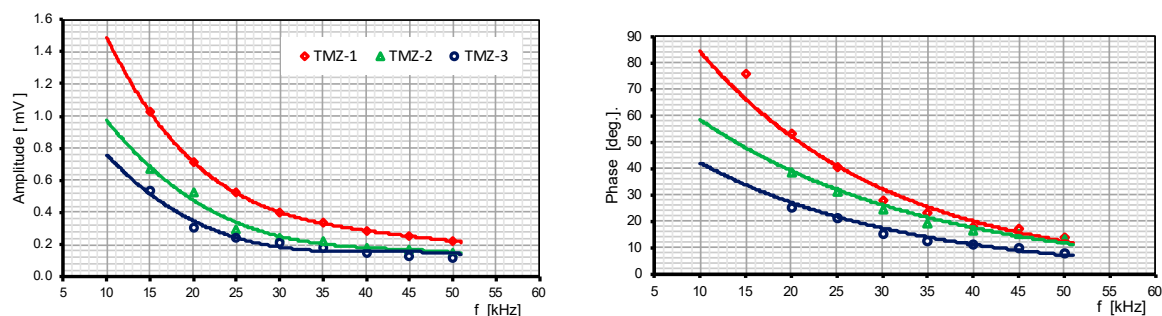
Figure 16. Amplitude and phase frequency dependence of TO for TMZ coatings.

Table 2. Values of thermal parameters of TMZ coatings determined using BDS.

Coating	Thermal Diffusivity $\alpha_c \times 10^{-3}$ (cm^2/s)	Thermal Conductivity $\lambda_c \times 10^{-3}$ (W/cm·K)
TMZ-I	2.53 ± 0.08	2.64 ± 0.09
TMZ-I/Ce	2.14 ± 0.07	2.21 ± 0.07
TMZ-II	2.44 ± 0.08	2.52 ± 0.08
TMZ-II/Ce	1.96 ± 0.06	2.02 ± 0.07
TMZ-III	2.05 ± 0.06	2.15 ± 0.07
TMZ-III/Ce	1.75 ± 0.05	1.87 ± 0.06

Thermal diffusivity decreases with an increase in zirconium in the coating (from TMZ-I to TMZ-III). The highest thermal diffusivity ($\alpha_c = 2.53 \times 10^{-3}$, cm^2/s) has the TMZ-I sample, containing the lowest amount of Zr (molar ratio of ZTP is 0.06). Thermal conductivity has the same tendency as thermal diffusivity. The results are in good agreement with the values obtained by the PTR method.

5.4. Correlation between Thermal Properties and Structural Properties

It is seen from the previous sections (Sections 5.2 and 5.3) that thermal diffusivity decreases with an increase in zirconium in the coating (from TMZ-I to TMZ-III). The highest thermal diffusivity is shown by the TMZ-I sample, containing the lowest amount of Zr (molar ratio of ZTP is 0.06). Thermal conductivity has the same tendency as thermal diffusivity. Due to the presence of Zr during the condensation process, large domains of polycondensed Si species are formed which introduces additional interfaces in the matrix material, thus deteriorating the rate of heat conduction and consequently its exchange with surroundings leading to decrease in the values of thermal properties of the coating.

The addition of Ce ions into the TMZ coatings leads to a further decrease in the values of their thermal parameters since the structural characteristics of the coatings are further changed as Ce forms a more condensed network by increasing the condensation rate of the hybrid sol by reducing the amount of silanol groups in the matrix and introducing crosslinking between polymer molecules. Furthermore, Ce ions are of larger size (1.978 Å) compared to silicon atoms (1.068 Å) and are able to migrate through the anticorrosion layer which may result in changes in its barrier properties by introducing lattice deformation and thus forming pores and cracks [49–51]. The results obtained by PTR and BDS methods are in good agreement.

6. Conclusions

The investigated sol–gel coatings were synthesized and deposited on the aluminum substrate. Their thermal parameters were investigated. The data show that different amounts of Zr in the siloxane network and the addition of Ce in Si/Zr sol led to their different thermal properties. These results were obtained with the use of PTR and BDS methods. It was proved that it was possible to determine simultaneously both the thermal diffusivity and thermal conductivity of the samples from the fitting of theoretical to experimental frequency amplitude and phase PTR as well as BDS characteristics. Thermal diffusivity values obtained by the PTR method are in the range $(1.838–2.404) \times 10^{-3}$ cm^2/s; on the other hand, the thermal conductivity values are in the range $(1.710 – 2.730) \times 10^{-3}$ W/cm·K. The values of the thermal diffusivity obtained using BDS are in the range $(1.75–2.53) \times 10^{-3}$ cm^2/s, and thermal conductivity values are in the range $(1.8–2.6) \times 10^{-3}$ W/cm·K. The new research aspect was the use of two nondestructive methods (PTR and BDS) and comparing the results obtained using these methods. The use of these methods allowed for precise determination of the obtained thermal parameters of the tested layers. The compliance of the results made them reliable. It was found that in both cases the thermal diffusivity decreased with an increase in the amount of Zr in the coating. Thermal conductivity had the same tendency as thermal diffusivity. It was also shown that the addition of Ce into the sol–gel coatings changed their physical properties. The thermal parameters also decreased with the addition of the cerium in the coating. In other words, the sample with the greater amount of incorporated zirconium and loaded with cerium (TMZ-III/Ce) had the smallest values of thermal properties (thermal conductivity and diffusivity). The SEM images show that the state of homogeneity improved with the increase in the amount of zirconium in the coating. This can be explained by the changes in the network structure affecting thermal parameters since Zr is built into the coating structure.

Author Contributions: Conceptualization, Ł.C.; methodology, Ł.C. and D.K.; software, Ł.C. and H.B.; formal analysis, Ł.C., M.M. and H.B.; investigation, Ł.C. and H.B.; resources, P.R. and I.M.; data curation, Ł.C. and D.K.; writing—original draft preparation, Ł.C. and H.B.; writing—review and editing, Ł.C., M.M., D.K., P.R., I.M. and S.J.-L.; visualization, Ł.C. and H.B.; supervision, Ł.C. and D.K. All authors have read and agreed to the published version of the manuscript.

Conflicts of Interest: The authors declare no conflict of interest.

References

1. Rodič, P.; Iskra, J.; Milošev, I. Study of a sol-gel process in the preparation of hybrid coatings for corrosion protection using FTIR and 1H NMR methods. *J. Non-Cryst. Solids* **2014**, *396–397*, 25–35. [CrossRef]
2. Associates, D.; Davis, J.R. Alloying: Understanding the basics. *Choice Rev. Online* **2013**. [CrossRef]
3. Rodič, P.; Milošev, I. Corrosion properties of UV cured hybrid sol-gel coatings on AA7075-T6 determined under simulated aircraft conditions. *J. Electrochem. Soc.* **2014**, *161*, C412–C420. [CrossRef]
4. Rodič, P.; Milošev, I. Electrochemical and salt spray testing of hybrid coatings based on Si and Zr deposited on aluminum and its alloys. *J. Electrochem. Soc.* **2015**, *162*, C592–C600. [CrossRef]
5. Rodič, P.; Mertelj, A.; Borovšak, M.; Benčan, A.; Mihailović, D.; Malič, B.; Milošev, I. Composition, structure and morphology of hybrid acrylate-based sol–gel coatings containing Si and Zr composed for protective applications. *Surf. Coat. Technol.* **2016**, *286*, 388–396. [CrossRef]
6. Rodič, P.; Milošev, I. Corrosion inhibition of pure Aluminium and alloys AA2024-T3 and AA7075-T6 by Cerium(III) and Cerium(IV) salts. *J. Electrochem. Soc.* **2016**, *163*, C85–C93. [CrossRef]
7. Figueira, R.B.; Silva, C.J.R.; Pereira, E.V. Organic–inorganic hybrid sol–gel coatings for metal corrosion protection: A review of recent progress. *J. Coat. Technol. Res.* **2015**, *12*, 1–35. [CrossRef]
8. Rodič, P.; Katić, J.; Korte, D.; Desimone, P.M.; Franko, M.; Ceré, S.M.; Metikoš-Huković, M.; Milošev, I. The Effect of Cerium Ions on the Structure, Porosity and Electrochemical Properties of Si/Zr-Based Hybrid Sol-Gel Coatings Deposited on Aluminum. *Metals* **2018**, *8*, 248. [CrossRef]
9. Milošev, I.; Hamulić, D.; Rodič, P.; Carrière, C.; Zanna, S.; Budasheva, H.; Korte, D.; Franko, M.; Mercier, D.; Seyeux, A.; et al. Siloxane polyacrylic sol-gel coatings with alkly and perfluoroalkyl chains: Synthesis, composition, thermal properties and log-term corrosion protection. *Appl. Surf. Sci.* **2022**, *574*, 151578. [CrossRef]
10. Rhee, S.K. Porosity-thermal conductivity correlations for ceramic materials. *Mater. Sci. Eng.* **1975**, *20*, 89–93. [CrossRef]
11. Moron-Fernandez, C.; Verdu-Vazquez, A.; Gil-Lopez, T.; Moron-Barrios, A. Microscope stand for the measurement and characterization of amorphous ferromagnetic materials. *IEEE Trans. Instrum. Meas.* **2021**, *70*, 9440877. [CrossRef]
12. Zhang, J.-Q.; Qi, H.; Liu, S.-B.; Niu, Z.-T.; Yu, X.-Y.; Ren, Y.-T. Research on modulated thermal wave radar imaging technique for photothermal properties of semi-transparent materials. *Int. J. Thermophys.* **2020**, *41*, 63. [CrossRef]
13. Li, G.; Li, C.; Xing, Z.; Wang, H.; Huang, Y.; Guo, W.; Liu, H. Study of the catalytic strengthening of a vacuum carburized layer on alloy steel by rare earth pre-implantation. *Materials* **2019**, *12*, 3420. [CrossRef] [PubMed]
14. Nordal, P.-E.; Kanstad, S.O. Photothermal radiometry. *Phys. Scr.* **1979**, *20*, 659–662. [CrossRef]
15. Salnic, A.; Mandelis, A.; Jean, C. Noncontact measurement of transport properties of long–carrier–lifetime wafers using photothermal radiometry. *Appl. Phys. Lett.* **1996**, *69*, 2522–2524. [CrossRef]
16. Salnik, A.; Mandelis, A.; Ruda, H.; Jean, C. Relative sensitivity of photomodulated reflectance and photothermal infrared radiometry to thermal and carrier plasma waves in semiconductors. *Appl. Phys. Lett.* **1997**, *82*, 1853–1859. [CrossRef]
17. Mandelis, A. Laser infrared photothermal radiometry of semiconductors: Principles and applications to solid state electronics. *Solid-State Electron.* **1998**, *42*, 1–15. [CrossRef]
18. Pham Tu Quoc, S.; Cheymol, G.; Semerok, A. New contactless method for thermal diffusivity measurements using modulated photothermal radiometry. *Rev. Sci. Instrum.* **2014**, *85*, 054903. [CrossRef]
19. Pelzl, J.; Kijamnajsuk, P.; Chirtoc, M.; Horny, N.; Eisenmenger-Sittner, C. Correlation between thermal interface conductance and mechanical adhesion strength in Cu-coated glassy Carbon. *Int. J. Thermophys.* **2015**, *36*, 2475–2485. [CrossRef]
20. Kijamnajsuk, P.; Pelzl, J.; Chirtoc, M.; Horny, N.; Schäfer, D.; Eisenmenger-Sittner, C. Photothermal evidence of laterally inhomogeneous interfacial thermal resistance in Copper-coated carbon samples. *Int. J. Thermophys.* **2012**, *33*, 2132–2138. [CrossRef]
21. Pawlak, M.; Kruck, T.; Spitzer, N.; Dziczek, D.; Ludwig, A.; Wieck, A. Experimental validation of formula for calculation thermal diffusivity in superlattices performed using a combination of two frequency-domain methods: Photothermal infrared radiometry and thermoreflectance. *Appl. Sci.* **2021**, *11*, 6125. [CrossRef]
22. Chrobak, Ł.; Maliński, M. Investigations of the possibility of determination of thermal parameters of Si and SiGe samples based on the Photo Thermal Radiometry technique. *Infrared Phys. Technol.* **2018**, *89*, 46–51. [CrossRef]
23. Pawlak, M.; Maliński, M. Simultaneous measurement of thermal diffusivity and effective infrared absorption coefficient in IR semitransparent and semiconducting n-CdMgSe crystals using photothermal radiometry. *Thermochim. Acta* **2015**, *599*, 23–26. [CrossRef]
24. Pawlak, M. Photothermal, photocarrier, and photoluminescence phenomena in semiconductors studied using spectrally resolved modulated infrared radiometry: Physics and applications. *J. Appl. Phys.* **2019**, *126*, 150902. [CrossRef]
25. Chrobak, Ł.; Maliński, M. Comparison of three non-destructive and contactless techniques for investigations of recombination parameters on an example of silicon samples. *Infrared Phys. Technol.* **2018**, *91*, 1–7. [CrossRef]
26. Chrobak, Ł.; Maliński, M. On Investigations of the optical absorption coefficient of Gold and germanium implanted silicon with the use of the non-destructive contactless photo thermal infrared radiometry. *J. Electron. Mater.* **2019**, *48*, 5273–5278. [CrossRef]
27. Dorywalski, K.; Chrobak, Ł.; Maliński, M. Comparative studies of the optical absorption coefficient spectra in the implanted layers in silicon with the use of non-destructive spectroscopic techniques. *Metrol. Meas. Syst.* **2020**, *27*, 323–337.

28. Kesmia, A.; Satour, F.Z.; Zegadi, A. Spectral absorption coefficient extraction of an unknown layer from photoacoustic measurements of multilayered semiconductors. *Infrared Phys. Technol.* **2020**, *108*, 103348. [CrossRef]

29. Volkov, D.S.; Rogova, O.B.; Proskurnin, M.A. Photoacoustic and photothermal methods in spectroscopy and characterization of soils and soil organic matter. *Photoacoustics* **2020**, *17*, 100151. [CrossRef]

30. Dubyk, K.; Pastushenko, A.; Nychyporuk, T.; Burbelo, R.; Isaiev, M.; Lysenko, V. Thermal conductivity of silicon nanomaterials measured using the photoacoustic technique in a piezoelectric configuration. *J. Phys. Chem. Solids* **2019**, *126*, 267–273. [CrossRef]

31. Riech, I.; Zambrano, M.; Abelenda, A.; Maldonado, F.; Rojas-Marroquín, A.; Jaime, J.; Calderón, A.; Marín, E. Evaluation of thin films intermixing by photoacoustic spectroscopy. *Thin Solid Film.* **2021**, *735*, 138871. [CrossRef]

32. Maliński, M.; Chrobak, Ł.; Patryn, A. Theoretical and experimental studies of a plasma wave contribution. *Acta Acust. United Acust.* **2009**, *95*, 60–64. [CrossRef]

33. Chrobak, Ł.; Maliński, M.; Patryn, A. Influence of plasma waves on the photoacoustic signal of silicon samples. *Int. J. Thermophys.* **2011**, *32*, 1986–1997. [CrossRef]

34. Strzałkowski, K. Effect of lattice disorder on the thermal conductivity of ZnBeSe, ZnMgSe and ZnBeMgSe crystals. *Mater. Chem. Phys.* **2015**, *163*, 453–459. [CrossRef]

35. Strzałkowski, K. Thermal properties of selected II–VI semiconductors determined by photopyroelectric calorimetry technique. *J. Therm. Anal. Calorim.* **2021**, *145*, 227–244. [CrossRef]

36. Leahu, G.; Petronijevic, E.; Li, R.; Belardini, A.; Cesca, T.; Mattei, G.; Sibilia, C. Diffracted beams from metasurfaces: High chiral detectivity by photothermal deflection technique. *Adv. Opt. Mater.* **2021**, *9*, 2100670. [CrossRef]

37. Cabrera, H.; Korte, D.; Budasheva, H.; Asbaghi, B.A.N.; Bellucci, S. Through-plane and in-plane thermal diffusivity determination of graphene nanoplatelets by photothermal beam deflection spectrometry. *Materials* **2021**, *14*, 7273. [CrossRef]

38. Hadi, M.; Younes, J.; Soueidan, M.; Kazan, M. IR photothermal and spectroscopic analysis of proton-irradiated 4H-SiC. *Infrared Phys. Technol.* **2021**, *118*, 103891. [CrossRef]

39. Kusiak, A.; Martan, J.; Battaglia, J.L.; Daniel, R. Using pulsed and modulated photothermal radiometry to measure the thermal conductivity of thin films. *Thermochim. Acta* **2013**, *556*, 1–5. [CrossRef]

40. Battaglia, J.-L.; Ruffio, E.; Kusiak, A.; Pradere, C.; Abisset, E.; Chevalier, S.; Sommier, A.; Batsale, J.-C. The periodic pulse photothermal radiometry technique within the front face configuration. *Measurement* **2020**, *158*, 107691. [CrossRef]

41. Almond, D.P.; Patel, P. *Photothermal Science and Techniques*; Chapman & Hall: London, UK, 1996.

42. Rosencwaig, A.; Gersho, A. Theory of the photoacoustic effect with solids. *J. Appl. Phys.* **1976**, *47*, 65–69. [CrossRef]

43. Bennett, C.A.; Patty, R.R. Thermal wave interferometry: A potential application of the photoacoustic effect. *Appl. Opt.* **1982**, *21*, 49–58. [CrossRef]

44. Korte, D.; Franko, M. Application of complex geometrical optics to determination of thermal, transport, and optical parameters of thin films by the photothermal beam deflection technique. *J. Opt. Soc. Am. A* **2014**, *32*, 61–74. [CrossRef]

45. Lim, J.T.; Choi, J.-G.; Bak, H.Y.; Park, S.-H.; Kim, U. Photoacoustic investigation of the carrier transport processes and the thermal properties in n-type GaAs. *J. Korean Phys. Soc.* **1997**, *31*, 608–612.

46. Glorieux, C.; Thoen, J. Thermal depth profile reconstruction by neural network recognition of the photothermal frequency spectrum. *J. Appl. Phys.* **1996**, *80*, 6510–6515. [CrossRef]

47. Williams, J.H. *Quantifying Measurement*; Morgan & Claypool Publishers: San Rafael, CA, USA, 2016; ISBN 978-1-6817-4433-9/978-1-6817-4432-2.

48. Kirkup, L.; Frenkel, R.B. *An Introduction to Uncertainty in Measurement: Using the GUM (Guide to the Expression of Uncertainty in Measurement)*; Cambridge University Press: Cambridge, UK, 2010; ISBN 978-0-5117-5553-8.

49. Andreeva, D.V.; Shchukin, D.G. Smart self-repairing protective coatings. *Mater. Today* **2008**, *11*, 24–30. [CrossRef]

50. Druart, M.-E.; Recloux, I.; Thai, T.T.; Ershov, S.; Snyders, R.; Olivier, M.-G. Impact of the addition of cerium salts (Ce(III) and Ce(IV)) on formation and ageing of a silica sol-gel layer. *Surf. Coat. Technol.* **2016**, *304*, 40–50. [CrossRef]

51. Cambon, J.-B.; Esteban, J.; Ansart, F.; Bonino, J.-P.; Turq, V.; Santagneli, S.H.; Santilli, C.V.; Pulcinelli, S.H. Effect of cerium on structure modifications of a hybrid sol–gel coating, its mechanical properties and anti-corrosion behavior. *Mater. Res. Bull.* **2012**, *47*, 3170–3176. [CrossRef]